Multiscale Modeling as a Tool for the Prediction of Catalytic Performances: The Case of n-Heptane Hydroconversion in a Large-Pore Zeolite

Jean-Marc Schweitzer, Jérôme Rey, Charles Bignaud, Tomáš Bučko, Pascal Raybaud, Maïlys Moscovici-Mirande, Frédéric Portejoie, Christophe James, Christophe Bouchy, Céline Chizallet

Multiscale Modeling as a Tool for the Prediction of Catalytic Performances: The Case of *n*-Heptane Hydroconversion in a Large-Pore Zeolite

Jean-Marc Schweitzer,* Jérôme Rey, Charles Bignaud, Tomáš Bučko, Pascal Raybaud, Maïlys Moscovici-Mirande, Frédéric Portejoie, Christophe James, Christophe Bouchy, and Céline Chizallet*

ABSTRACT: The optimization of predictive kinetic models for catalytic processes is a topical challenge. In the present work, a predictive multiscale single-event microkinetic model based on the data obtained by density functional theory (DFT) calculation for *n*-heptane hydroconversion in large-pore zeolites has been obtained. It was validated by a large set of kinetic data obtained by high-throughput kinetic experiments, performed with a well-balanced Pt/Beta zeolite catalyst. DFT calculations show that secondary cations are much less stable than tertiary cations and adsorbed alkenes. This is of prime importance in the quantification of type B isomerization reaction barriers depending on the type of the carbenium ion. Cracking reaction barriers are also strongly affected by the nature of the cation that cracks and that of the cracking products. The agreement between simulated and experimental kinetic data is satisfactory, showing the reliability of the multiscale kinetic approach. Only a few parameters were adjusted to improve the correspondence with experiments. The analysis of the simulated coverage demonstrates a very low proportion of acidic sites involved in the adsorption and further reactions in the relevant experimental conditions. When these occur, tertiary carbenium ion intermediates appear in a significantly higher concentration with respect to other species. This works opens the route to a better prediction of the catalytic performance of large-pore zeolites in alkane hydroconversion.

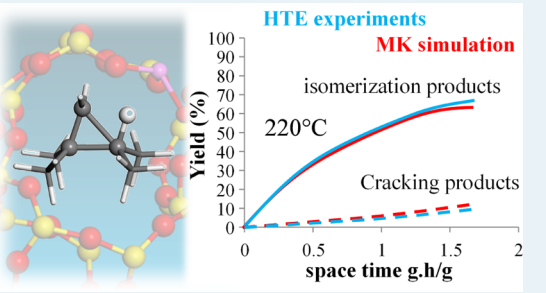

KEYWORDS: *hydroisomerization, alkene, zeolite, density functional theory, kinetic modeling, multiscale modeling*

1. INTRODUCTION

The knowledge of reaction mechanisms and the quantification of the reaction kinetics are of paramount importance in the optimization of catalytic processes. Usual kinetic modeling approaches rely first on experimental kinetic measurements in a given operating condition window before fitting of a model with a variable degree of details.[1] Single-event kinetic modeling appeared to be fruitful in the case of many catalytic applications, in particular for the hydroconversion of alkanes on bifunctional catalysts, containing a metallic and an acidic phase.[2−5] The latter is often a zeolite. However, such approaches encounter some limitations in terms of relevance of the chosen mechanisms and of extrapolation to other operating conditions with respect to the one sampled. These difficulties can be assigned to the significant number of a priori unknown rate constants, making it possible to have good fitting results for several sets of models based on various mechanistic proposals. Notably, the more abundant the kinetic experimental data are, the more accurate (and likely, predictive) the kinetic model will be, but obtaining such detailed data is time-consuming in a traditional approach of kinetic data recording.

First-principles calculations (such as wave function or density functional theory (DFT) based ab initio calculations) bring very useful information at the atomic scale about the nature of the active sites on the catalysts, the most likely intermediates, and transition states.[6] Relevant mechanisms may thus be proposed, and free energy profiles can be quantified along various pathways. For complex reaction networks, however, besides the computational cost limitation, it is not trivial to conclude about the preferred catalytic routes. Indeed, each single route consists of a set of elementary steps, with limiting intermediates and transition states. Comparing all routes requires the quantification of their effective rates, that is, a combination of the rates of each elementary step.

Hence, a multiscale simulation approach may be proposed for deciphering the reaction mechanisms by kinetic modeling, benefiting from the atomic scale information delivered by first-principles approaches. The mechanisms determined by quantum chemistry calculations are the basis of the reaction network to be considered. The rate constants that are obtained by the first-principles approach may be used as input data without a fitting procedure. The comparison with reference experimental data remains important first to check the validity of the approach, second to fit a few rate or equilibrium constants that have not been determined by first-principles calculations. This approach has been fruitfully undertaken for several catalytic systems.[7−10] However, the applications to zeolite-catalyzed reactions have been rather scarce, and the comparison with experimental data did not always lead to a full compatibility.[11−16]

In the present work, we address the case of *n*-heptane hydroconversion on a bifunctional Pt-zeolite catalyst. From an industrial point of view, the hydroconversion of alkanes is a highly important process for the production of fuels, both starting from conventional resources or from renewables.[17−20] From a fundamental point of view, alkane hydroisomerization, in particular, that of *n*-heptane, is a commonly used tool for the understanding of the effect of the metal−acid site distance on the isomerization versus cracking selectivity, in link with the topology of the aluminosilicate hosting the acid sites.[21−27] Single-event kinetic modeling has also been extensively applied to the hydroisomerization of alkanes on bifunctional catalysts.[2−5] The reaction is expected to start by the dehydrogenation of heptane into linear heptenes. The latter then diffuses toward the acid sites, adsorbs on it in the form of a π-complex, and is protonated by the Brønsted acid site of the zeolite. Although the most likely form of the protonated species (alkoxides vs carbenium ions) was debated for decades and is still debated today,[28−32] we will consider here carbenium ions as the core of the reaction network as dynamic effects were shown to stabilize them and as the extra activation barriers (with respect to thermodynamic limitations) for the interconversion between π-complexes, alkoxides, and carbenium ions are low.[33−37] Carbenium ions then undergo isomerization reactions, classified as a function of the change in the branching degree.[17,38] Type A isomerization reactions do not change the branching degrees as a result of alkyl or hydride shifts. Type B isomerization reactions result in a change of the branching degree. The transition states were shown to be edge-protonated cyclopropanes (PCPs),[38−40] giving rise to the network depicted in Figure 1, restricted to type B isomerization reactions. Then, branched carbenium ions may undergo cracking reactions. In the case of C_7 alkanes, cracking reactions are classified along three types (Figure 2).[41] B_1 cracking transforms a secondary cation into a tertiary one, B_2 a tertiary into a secondary, and type C transforms a secondary carbenium ion into another secondary carbenium ion. In all cases, the C_7 ion is converted into a C_3 plus a C_4 ion/molecule. Notably, it was recently shown that the cracking reactions are not always limited only by the β-scission process but that additional free energy cost has to be paid when a secondary carbenium ion is formed to get the corresponding π-complex.[35] This will be considered in the following when choosing the rate constant for the cracking reactions. Finally, all the carbenium ions are expected to give their excess proton back to the zeolite products, and all alkenes diffuse back to the metal active phase, where they are hydrogenated. Starting from

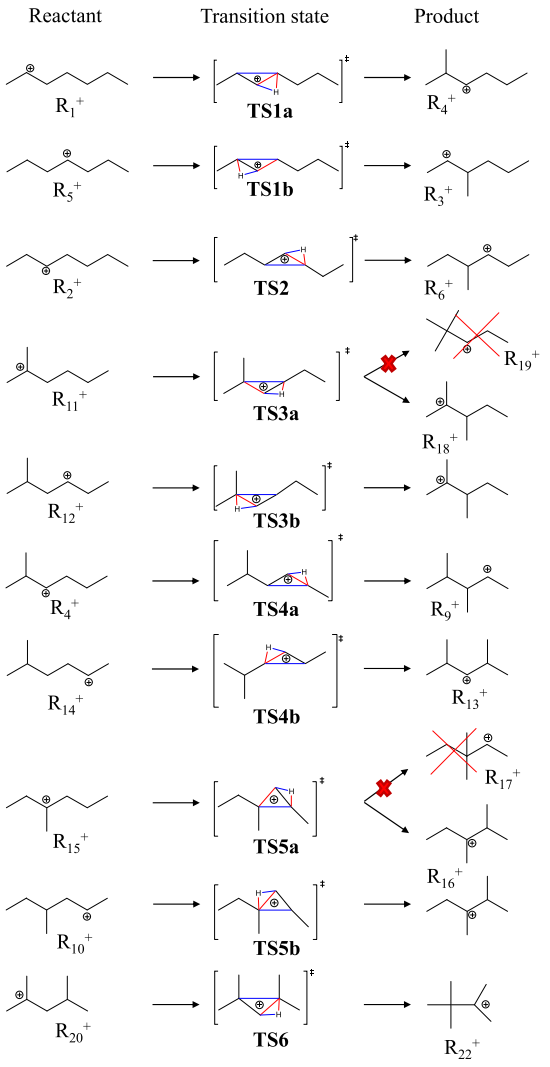

Figure 1. Type B isomerization network for C_7 carbenium ions depicted in the orientation that increases the branching degree. The terminology is adapted from ref 42. The red crosses depict the routes and products that were found in ref 42 to be impossible by the present DFT calculations. The edge position on the PCP transition state is explicitly given. The bonds that form and break in the forward direction are depicted in blue and red, respectively. The labeling of the carbenium ions corresponds to that used in the kinetic modeling (Section 3.3).

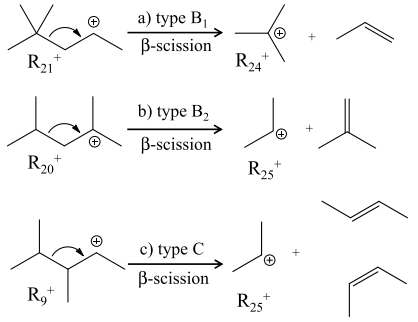

Figure 2. Usual classification of cracking reactions, valid for carbenium ions containing seven carbon atoms. The labeling of the carbenium ions corresponds to that used in the kinetic modeling (Section 3.3).

n-heptane as a reactant, a wide distribution of branched heptanes is expected, together with propane and butanes. The key properties that need to be well reproduced are the cracking over isomerization selectivity and the more detailed isomer distribution in terms of linear/monobranched/dibranched/tribranched/cracking products.

In the present work, we revisit kinetic modeling of this reaction network by proposing a multidisciplinary approach consisting of the following:

(i) the recording of massive and relevant experimental kinetic data obtained with the aid of high-throughput experimentation (HTE) used for the sampling of operation conditions for a unique catalyst. The latter contains platinum as the active phase, whereas the acid phase is a Beta zeolite as a representative of the large-pore (12 MR) zeolites. The catalyst is chosen to be well balanced in terms of bifunctionality, meaning that the hydro−dehydrogenation reactions are at equilibrium, whereas the kinetic limiting steps are the ones taking place at the acid sites.

(ii) the first-principles (quantum chemistry, at the DFT level) calculations of the relevant equilibrium and rate constants for each elementary step taking place in the zeolite. Several computational approaches are combined (static gas-phase calculations together with static and molecular dynamics calculations in a large-pore zeolite framework compatible with the computational demand, namely, CHA) to provide relevant rate constants for isomerization and cracking reactions catalyzed by large-pore zeolites.

(iii) the construction of a multiscale single-event model. Most rate constants are not fitted but come directly from DFT. The performance of the model is directly compared to HTE results to assess the validity of the prediction approach and deduce mechanistic characteristics.

2. EXPERIMENTAL PART AND METHODS

2.1. Experiments. *2.1.1. Catalytic Material.* The Beta zeolite was provided by Zeolyst (commercial reference CP811.E) and used as received for subsequent catalyst preparation. The Beta zeolite was loaded with 1 wt % of platinum to obtain a well-balanced bifunctional catalyst. Further evidence was obtained about the limitation of reaction kinetics by the acid phase, as reported in Supporting Information S1. To obtain a well-balanced bifunctional catalyst, incipient wetness impregnation of an aqueous solution of hydrated tetraammineplatinum chloride $Pt(NH_3)_4Cl_2{\cdot}H_2O$ was performed. After maturation, the impregnated material was dried in an oven at 120 °C overnight and then pelletized, crushed, and sieved in order to obtain particles with the diameter ranging from 200 to 355 μm. The sieved material was then calcined under air flow (2 NL per gram per hour) at 450 °C for 1 h.

The number of acid sites was determined via two different approaches. In the first approach described in ref 43, X-ray fluorescence (XRF, Thermo ScientificARL Perform'X) was used to determine the global Si/Al molar ratio (equal to 13, meaning 1389 μ_{mol} g^{-1} of aluminum). ^{27}Al magic-angle spinning nuclear magnetic resonance (MAS NMR, Bruker Ultrashield 400 MHz spectrometer, 4 mm CP MAS probe head, 12 kHz MAS rate, zg sequence, 0.5 s delay time) was employed to determine the percentage of framework and extra-framework aluminum. Na residual presence, measured by atomic absorption spectroscopy was taken into account in the estimation of the number of Brønsted acid sites as the number of framework Al_{IV} sites ($Si/Al_{IV\text{-framework}}$ = 16) minus the number of Na (0.23 wt %). A final value of 810 μmol g^{-1} was obtained. In the second approach, the number of Brønsted acid sites was determined by pyridine adsorption monitored by Fourier transform infrared (FTIR) spectroscopy. After activation under secondary vacuum for 10 h at 450 °C, the sample was kept in contact with pyridine (ca. 20 mbar equilibrium) at room temperature for 10 min and then at 150 °C for 10 min. The concentration of Brønsted acid sites (pyridinium concentration from the contribution at ca. 1545 cm^{-1}) was deduced after thermodesorption during 2 h at 150 °C and from the extinction coefficient of Emeis.[44] The final value was 116 μmol g^{-1}, much lower than that obtained from the XRF-NMR analysis, showing a high uncertainty in the number of Brønsted acid site evaluation.

2.1.2. Catalytic Testing. The catalytic testing was performed in an Avantium Flowrence unit, running 16 parallel fixed-bed reactors. The stainless-steel reactors (internal diameter 2.6 mm) were loaded with various amounts of the Pt/Beta catalyst. The amount of the loaded catalyst ranged from 50 to 550 mg. Four reactors were loaded with the same amount of the catalyst to evaluate the reproducibility of the results. Reproducibility was excellent as the conversion uncertainty was ± 1%. The operating conditions of each reactor were monitored individually, and the catalytic test was fully automated. An on-line gas chromatograph equipped with two flame ionization detectors and two low-polarity capillary columns CP Sil 5 CB was used to analyze the hydrocarbon products. At the beginning of the test, each catalyst was heated under hydrogen flow, with a heating rate of 5 °C min^{-1}, up to 723 K for an hour to perform *in situ* reduction. A set of various experimental conditions were explored to acquire valuable data for kinetic modeling. The space time, total pressure, temperature, and inlet hydrogen-to-*n*-heptane molar ratio were varied. The absence of significant hydrodynamic effect was checked experimentally (Supporting Information S2) and theoretically. As the size of catalyst particles was in the 200−350 μm range, the absence of intragranular diffusion phenomenon within the particles was assumed. During the test, the catalysts were evaluated periodically under reference conditions to check for any deactivation phenomenon. Deactivation was found to be negligible. 270 operating conditions were used for the validation of the kinetic model (return points included). Figure 3 shows how these conditions are distributed over space time and temperature ranges.

2.2. Density Functional Theory. Periodic DFT calculations were performed with the Perdew, Burke, and Ernzerhof (PBE) exchange−correlation[45] as implemented in VASP.[46,47] The projected augmented wave (PAW) method[48] was used to describe the core−electron interactions, and the plane-wave basis set was limited to a kinetic cutoff energy of 400 eV. Dispersion corrections as proposed within the D2 Grimme formalism[49] were applied. The convergence criterion for the electronic self-consistent field relaxation was fixed to 10^{-7} eV. All calculations were performed at the gamma point. In atomic relaxations of minima and saddle points, the structures were considered as relaxed when all forces acting on the atoms were smaller than 0.005 eV/Å.

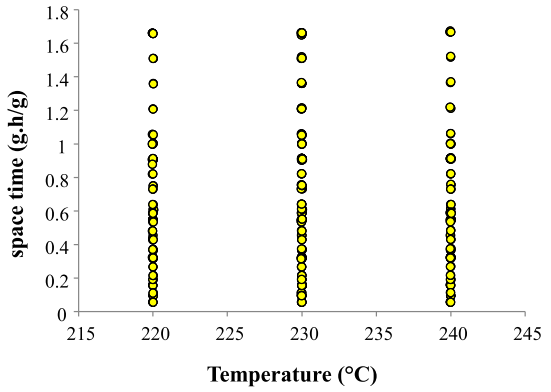

Figure 3. Operating conditions used in HTE testing for the validation of the kinetic model.

In a previous work, the static estimation of free energies of isolated carbenium ions and type A/B isomerization transition states was shown to be relevant in comparison with ab initio molecular dynamics (AIMD) estimates of the same species in a large cage zeolite.[40] Thus, as generalizing an AIMD approach for the whole type B isomerization network of C_7 alkenes is currently not feasible due to computational time constraints, we chose to rely on a static approach of isolated charged species (species depicted in Figure 1) with the cells of the same size and shape as in refs 39 and 40. The charge neutrality of the simulation cell has been preserved by using a compensating uniform background charge. The first-order saddle points on the potential-energy surface corresponding to the transition state were identified using the improved dimer method.[50,51] Subsequently, the intrinsic reaction coordinate[52,53] (IRC) for the forward and backward reaction steps was identified using the damped velocity Verlet algorithm.[54] Finally, the vibrational eigen spectrum of the structures corresponding to stationary points has been examined to ensure that the computed eigen spectrum contains a correct number of imaginary vibrational frequencies (zero for stable structures and one for transition states). The forward and backward activation enthalpy ($\Delta_rH_+^{\ddagger}$ and $\Delta_rH_-^{\ddagger}$, respectively) and entropy ($\Delta_rS_+^{\ddagger}$ and $\Delta_rS_-^{\ddagger}$, respectively) for each type B isomerization reaction were deduced by the harmonic approximation.[55] In this framework, the vibrational Gibbs energy, G, is identical to the vibrational Helmholtz free energy, A. Consequently, for monomolecular gas-phase reactions, Gibbs energy differences ΔG can be assimilated to the computed free energy differences ΔA.[55]

The equilibrium free energy for the adsorption of a C_7 alkene (4-methylhex-1-ene) as a π-complex from the gas phase was estimated by a static approach on a model of a large-cage zeolite of the CHA structure type (same cell as in ref 39). The equilibrium free energy for the protonation of π-complexes into secondary and tertiary carbenium ions was deduced from previous AIMD results.[35,39] The AIMD estimates of the type B1 and B2 free energy barriers were also obtained from a previous work.[35] Notably, due to its large structural model making accurate AIMD simulations intractable, we have not undertaken systematic calculations with the zeolite Beta. As a reasonable proxy for a large-void zeolite, we instead used the CHA framework which also has a large cage approaching the one found in zeolite Beta, as discussed in ref 35.

The equilibrium and rate constants (K and k) at T = 227 °C were deduced by the law of mass action (eq 1) and Eyring's equation[56] (eq 2, with T in Kelvin).

$$K = \exp\left(\frac{-\Delta_rG}{RT}\right) = \exp\left(\frac{-\Delta_rH + T\Delta_rS}{RT}\right) \quad (1)$$

$$k = \frac{k_BT}{h}\exp\left(\frac{-\Delta_rG^{\ddagger}}{RT}\right) = \exp\left(\frac{-\Delta_rH^{\ddagger} + T\Delta_rS^{\ddagger}}{RT}\right) \quad (2)$$

2.3. Kinetic and Reactor Modeling. A reaction scheme was developed at the level of elementary steps to be able to implement the kinetic parameters obtained from the DFT calculations. The complete hydrocracking reaction network of *n*-heptane was generated using the single-event methodology.[57−59] This approach consists in generating the whole set of possible reactions, respecting the carbenium ion chemical rules:[41]

- Type A isomerization reactions without changes in the number of branching (hydride shifts, methyl, and ethyl shifts)
- Type B isomerization reactions with changes in the number of branching by PCP and PCB (protonated cyclobutane)
- Cracking by β-scission.

The whole reaction scheme for the hydrocracking of *n*-heptane is given in Figure S4. The modeling strategy will be further detailed in Section 3.3.1. To predict the composition of the effluents at the reactor outlet as a function of the operating conditions, the microkinetic model must be integrated into a reactor model. A number of assumptions were used to build the reactor model. These hypotheses have been verified and validated experimentally on the HTE unit used. The hypotheses involve the following:

- The reactor is a gas−solid system
- The gas is considered to be in plug flow (Peclet > 20)
- The reactor works in isothermal conditions (good heat transfer between the wall and the gas due to the small reactor size 2.6 mm diameter)
- The reactor works in isobaric conditions (low pressure drop due to the small bed height of 6.9 cm)

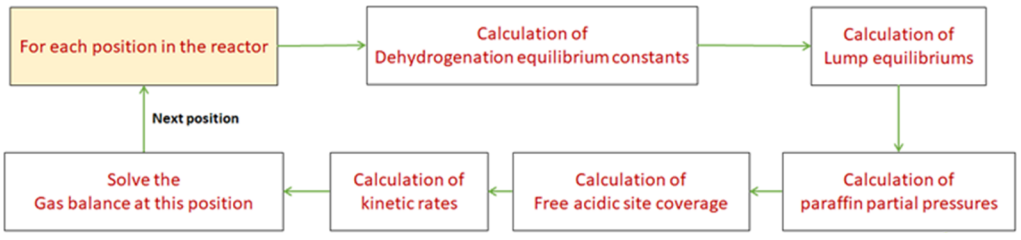

Figure 4. Reactor model algorithm including the microkinetic model.

- No external mass transfer limitations (negligible if H_{bed}/dp > 100,[60] here H_{bed}/dp = 230, where H_{bed} is the height of the catalyst bed and dp is the particle diameter).
- No intragranular diffusional limitations (small size of the catalyst, particle dp = 300 μm; Thiele's criterion is far below 1). Therefore, the mass balance[61] for each species in the gas phase can be deduced as follows (see the Nomenclature for the meaning of each term):

$$\frac{\partial F_i^g}{\partial z} = C_{site}^A \sum_j \mu_{ij} \cdot r_j \cdot S_r \cdot \rho_s \cdot \varepsilon_s \quad (3)$$

To solve this equation, a finite-difference discretization scheme was used. During the integration, a thermodynamic equilibrium calculation was performed at each axial position of the reactor to redistribute the isomers in the same group (see Sections 3.3.1 and 3.3.2). The model algorithm is given in Figure 4.

3. RESULTS AND DISCUSSION

3.1. Experimental Catalytic Features. *3.1.1. Apparent Reaction Scheme.* To establish an apparent reaction scheme, the isomers were lumped according to their branching degree (monobranched, dibranched, and tribranched) and cracked products were treated in a similar way. The evolution of the various lumps with *n*-heptane conversion is depicted in Figure 5.

The isomers appear in the order monobranched, dibranched, and tribranched (2,2,3-trimethylbutane, abbreviated as 223-TMC_4). Note that, even if at a low amount (limited by thermodynamics), 223-TMC_4 tends to accumulate because its cracking by β-scission is very unfavorable. Cracking products appear at least as secondary products. The evolution of the various products of *n*-heptane conversion is in accordance with a consecutive mechanism depicted in Figure 6, as expected for a well-balanced catalyst. In this case, hydro/dehydrogenation steps or the migration of the olefinic intermediates between the acidic and metallic step do not impede the transformation of the olefinic intermediates. Direct β-scission of an *n*-heptene intermediate is unlikely to occur because of the low stability of the corresponding primary carbocations involved. Significant cracking occurs once the paraffin has been isomerized as the β-scission rate of a carbocation increases with its branching degree.[17] For example, carbocation R_{20}+ is much more prone to be cracked than carbocation R_1+ (see Figures 1 and 2).

3.1.2. Thermodynamic Considerations. It is well known that paraffin isomerization is an equilibrated reaction. This was confirmed experimentally during the catalytic process by plotting the percentage of *n*-heptane in the n- and iso-heptanes as a function of the contact time for a given temperature (Figure S5). The thermodynamic equilibrium is reached for a space time higher than about 0.8 h at 240 °C. Experimentally, the equilibrium is reached at 12% mol *n*-heptane in the *n*- and *iso*-heptanes, which is in a very good agreement with the thermodynamic value calculated from the Thermodynamic Research Center data from the NIST.[62] A closer attention was paid to the internal distribution of the heptane isomers according to their branching degree, that is, monobranched or dibranched. Within the monobranched isomers, the thermodynamic equilibrium is reached for *n*-heptane conversion as low as 15%. The molar percentage of 2-methyl-hexane within the monobranched isomers is stable at 48 mol percent, regardless of the *n*-heptane conversion value for a given temperature and inlet hydrogen and *n*-heptane partial pressures (Figures 7 and 8).

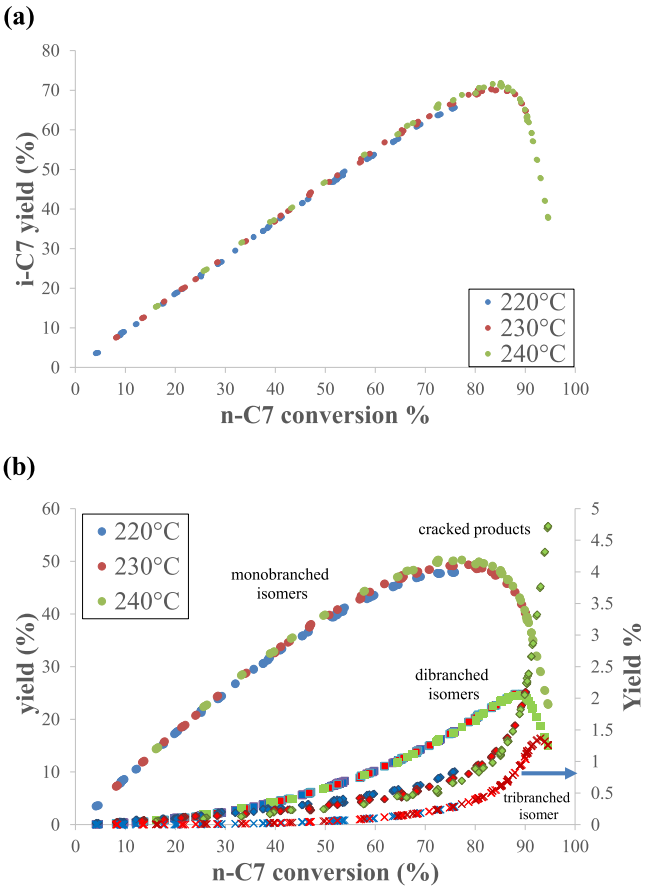

Figure 5. (a) Evolution of total isomers yield as a function of *n*-heptane conversion; (b) evolution of monobranched, dibranched, tribranched isomers, and cracked products as a function of *n*-heptane conversion. Tests were performed at 220, 230, and 240 °C, H_2/*n*-C_7 10 mol/mol, 10 barg, conversion varied with space time at each temperature.

3.2. DFT Calculations. Following the experimental observations, the rate constants were estimated by DFT for the main reactions catalyzed by the acid sites of the zeolite, namely, alkene isomerization and cracking reactions. Carbenium chemistry was shown to be at the core of the reaction network by recent AIMD calculations,[33−35,39,40] although the role of the alkenes adsorbed close to the acid sites, in the form of π-complexes, needs to be considered, in particular when discussing the properties of the secondary cations.[16,35,39] We note that since the reactions taking place at the platinum phase (dehydrogenation and hydrogenation reactions) were shown to be nonlimiting in the conditions explored, we did not consider these reactions in our DFT simulations, focusing on the kinetically relevant ones (acid-catalyzed reactions).

Thus, we considered the sequential reactions that occur starting from alkenes by DFT. The adsorption equilibrium constant of the 4-methylhex-1-ene from the gas phase to the acid site was computed to be $K_{ads}^{O_i}$ = 942.7 (adsorption free energy: −28 kJ/mol) at 227 °C (500 K) by a static approach (Table S1). The protonation of alkenes to carbenium ions is poorly described by static DFT approaches;[34] we therefore chose to use data obtained from AIMD (Table S2). While the free energies of tertiary carbenium ions and corresponding π-

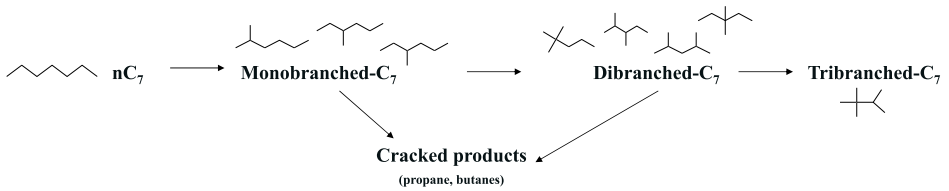

Figure 6. Apparent reaction scheme for *n*-heptane hydroconversion.

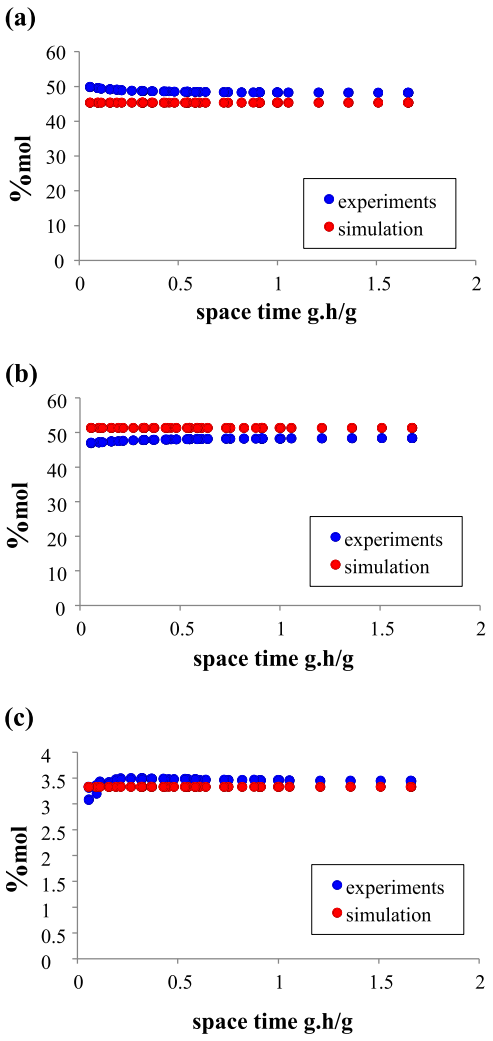

Figure 7. Relative molar composition of monobranched C_6 paraffins at 220 °C: (a) 3-methylhexane, (b) 2-methylhexane, and (c) 3-ethylpentane. Blue: experimental results, red: kinetic modeling results. Kinetic modeling results were obtained assuming a thermodynamic equilibrium between the monobranched species.

complexes are rather close, that of secondary carbenium ions is significantly higher (of the order of 45 kJ/mol at 227 °C), meaning that a fast transformation to the corresponding π-complexes is expected.

Type A isomerization reactions are known to be weakly activated, which was confirmed by AIMD[40] and by thermodynamic considerations discussed in Section 3.1.2. Thus, they are not the object of further DFT calculations in the present work. Type B isomerization reactions exhibit much higher free-energy barriers. The type B isomerization network was simulated by a static approach for isolated carbenium ions as it was shown that for one of these reactions, this compares well with the AIMD estimates in a large-cage zeolite.[40] In the present work, we generalize such an approach to the full type B isomerization network shown in Figure 1. The kinetic parameters for all reactions are gathered in Table S3, while the free energy of all the species is plotted in Figure 9. Transition states are all edge-protonated cyclopropanes (edge-PCPs), differing from one another in free energy by at most 15 kJ/mol. These PCPs are connected by IRC to the reactants and products. Most of these correspond to the expected species,[42] except for the two secondary carbenium ions where the charged carbon atoms are connected to a quaternary carbon atom (red crosses in Figure 1). These were not found to be local energy minima. Notably, a similar observation was reported in ref 33. In these two cases, a bifurcation to tertiary carbenium ions is observed, which corresponds to the breaking of alternative C−C bonds of the PCP. From a formal point of view, this corresponds to a spontaneous type A isomerization from a secondary to a tertiary carbenium ion. Tertiary carbenium intermediates are all much more stable than secondary carbenium ions (by about 50 kJ/mol). Here, again, among the members of each of the two families of ions, the free energy difference does not exceed 15 kJ/mol. These trends are also valid from an enthalpic point of view. The activation entropy (Table S3) is delimited by the interval of values between −14.1 and −45.6 J/mol/K, showing the tight nature of the transition states (TS).

According to the formalism of the kinetic model (see Section 3.3), the kinetic constants need to be lumped as a function of the branching degrees of the reactants and products, from linear to tribranched. The monobranched to dibranched conversion encompasses several cases depending on the secondary versus tertiary nature of the reactants/products. The results of the averaging performed to get these rate constants (average performed on activation enthalpies and entropies) are given in Tables S4 and S5. Considering carbenium ions as reactants and products, all steps starting from a secondary cation are much faster ($k \sim 10^8$ to 10^9 s^{-1}) than those starting from tertiary carbenium ions ($k \sim 10^3$ to 10^4 s^{-1}). Focusing on the steps starting from a secondary carbenium ion, the increase of the branching degree (linear → monobranched → dibranched) is faster than its decrease (reverse reactions). Moreover, the monobranched → dibranched is faster than the linear → monobranched, still considering secondary carbenium ions as intermediates. These trends are still valid for tertiary carbenium ions (except for the t → t for the monobranched → dibranched case, which is slower than the dibranched → monobranched). In particular, the dibranched → tribranched reaction is predicted to be faster than the monobranched → dibranched one.

The cracking reactions that need to be considered for C_7 alkenes are depicted in Figure 2. Cracking reactions cannot be simulated easily by a gas-phase approach, in particular when a secondary carbenium ion is produced: the reverse reaction appears to be too fast to lead to stable dissociated products.

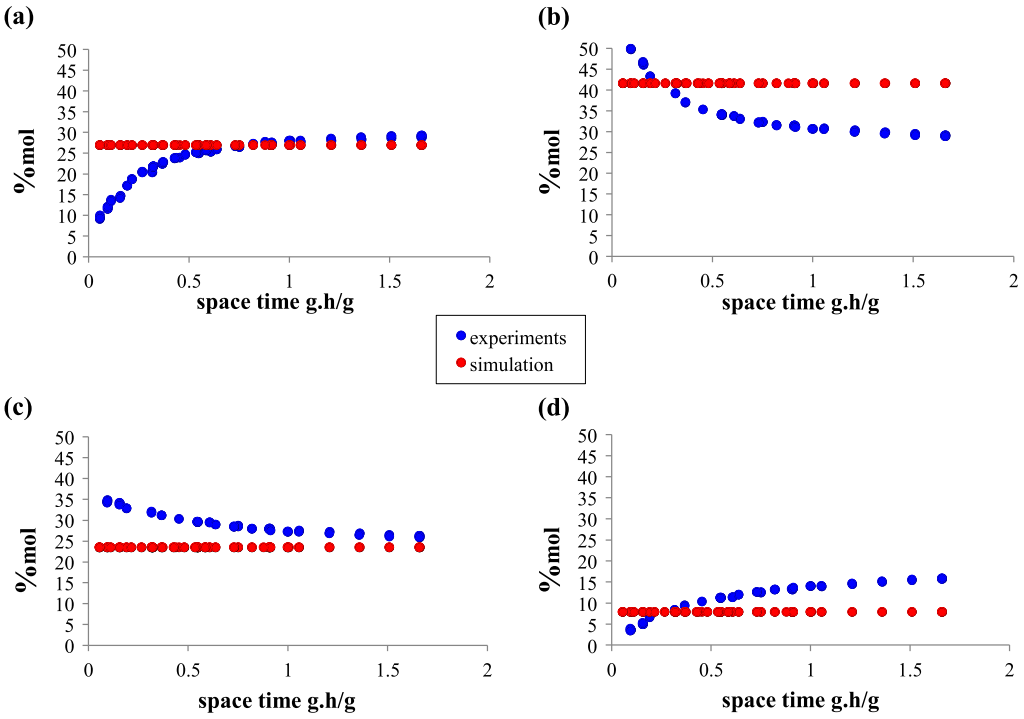

Figure 8. Relative molar composition of dibranched C6 paraffins at 220 °C: (a) 2,2-dimethylpentane, (b) 2,3-dimethylpentane, (c) 2,4-dimethylpentane, and (d) 2,5-dimethylpentane. Blue: experimental results, red: kinetic modeling results. Kinetic modeling results were obtained assuming a thermodynamic equilibrium between the dibranched species.

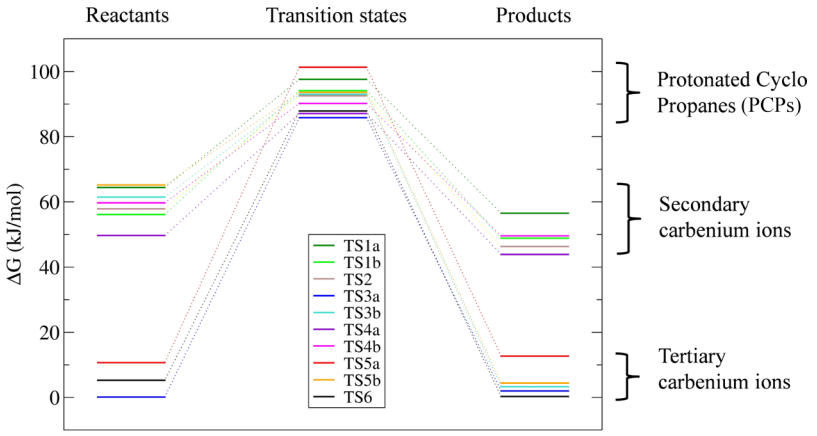

Figure 9. Free energy computed by DFT for all species depicted in Figure 1, linked by IRC calculations. The most stable system (R_{22}^+, see Figure 1) is assigned zero free energy.

This is likely related to the high-energy barrier for the B_2 cracking reaction found by AIMD, explained by the proton restitution to the zeolite network that occurs right after β-scission in the same elementary step.[35] Regarding B_1 β-scission, the charged product is the stable tertiary isobutenium cation, but the reactant is an unstable secondary cation, which was shown to be connected to a more stable π-complex.[35] The rate constants that can be deduced from this previous AIMD investigation can be found in Table S6. The rate constant for B_2 cracking (that starts from a tertiary carbenium ion) is of the same order of magnitude as the isomerization rate constant of tertiary cations (1.7×10^4 vs $\sim 10^3$ to 10^4 s^{-1}). Conversely, the rate constant for B_1 cracking (that starts from a secondary carbenium ion) is higher than that of type B isomerization reactions of secondary cations (2.8×10^{11} vs $\sim 10^8$ to 10^9 s^{-1}). This suggests that secondary cations likely promote the cracking of C_7 alkenes with respect to their type B isomerization.

3.3. Kinetic Modeling and Comparison with Experiments. *3.3.1. Modeling Strategy.* A single-event methodology was chosen. The whole reaction scheme for the hydrocracking of *n*-heptane is given in Figure S4. It involves 12 alkanes (paraffins), 31 alkenes (olefins), and 25 carbenium ions. Paraffins undergo 31 dehydrogenation reactions, whereas olefins undergo 31 hydrogenation and 44 protonation reactions. Carbenium ions undergo 26 hydride shifts, 8 methyl shifts, 4 ethyl shifts, 56 PCP branchings, 20 PCB branchings, 5 β-scissions, and 44 deprotonation reactions. As discussed in Section 3.2, isomerization reactions without a change in the number of branches (hydride, methyl, and ethyl shifts) are very fast compared to those with a change in the number of branches (isomerization by PCP and PCB).[40,41,57] Therefore, a

thermodynamic equilibrium can be assumed for paraffins with the same number of carbon atoms and branches. On the other hand, the reactions of isomerization by PCP and PCB are considered to be the rate-determining steps and must be considered in the microkinetic model.

Due to the complexity of the reaction network, the reaction scheme can be reduced in accordance with the assumptions of the thermodynamic equilibrium for some elementary steps (hydride, methyl, and ethyl shifts). Moreover, the number of olefins can also be reduced since one carbenium ion can be formed by two olefins issued from the same paraffin. In the example shown in Figure 10, both olefins have similar

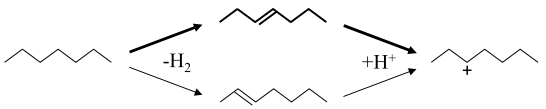

Figure 10. Carbenium ion issued from two C_7 olefins. The route depicted in bold (top) is the one retained in the lumping procedure for olefins.

thermodynamic properties. Therefore, both olefins can be grouped into one characteristic lump represented by only one of them (depicted in bold in Figure 10).

Figure 11 gives a summary of the chemical species which are taken into account for the reduced reaction scheme.

Finally, the reduced reaction scheme depicted in Figure 12 is obtained. The stoichiometry matrix is given in Figure S7.

In this final reaction scheme, only rate-determining steps such as isomerization reactions with a change in the number of branches (PCP and PCB) and β-scission reactions are considered. PCB reactions were eliminated since two consecutive PCPs lead to the same carbenium ion as a single PCB. Therefore, it becomes difficult to discriminate between both chemical routes because they cannot be sensitized with experiments. Moreover, the number of PCP reactions is predominating. This leads to a final set of 45 elementary steps: 40 PCP isomerization reactions and 5 β-scission reactions.

The relevant equations used for the kinetic model are gathered in Supporting Information S4. We use the data provided by ab initio calculations (Section 3.2 and Supporting Information S3) for most rate constants, summarized in Table 1, following a lumping strategy. For each reaction of the reaction network, the corresponding kinetic constant was assigned according to the type of carbenium ion involved (either secondary or tertiary). Note that the reaction giving a secondary dibranched ion from a tertiary monobranched ion was suggested to be nonexistent by the ab initio calculation, a type A isomerization product (tertiary dibranched ion) being spontaneously obtained at the end of the calculation. This was implemented in the kinetic model.

The Gibbs free energy of activation of the type C cracking reactions (transforming a secondary cation to an alkene and another secondary cation, Figure 2) was not determined by the ab initio calculations. Indeed, β-scissions cannot be relevantly simulated by static calculations, and previous AIMD investigations were conducted only for the type B_1 and B_2 cracking.[35] An estimate of this free energy was obtained by assuming that the transition state of such a transformation should resemble that of the B_2 cracking; as for the latter, a specific nature of the TS was shown to avoid the formation of the unstable secondary carbenium ion as a product. However, the barrier of the type C cracking is necessarily lower than that

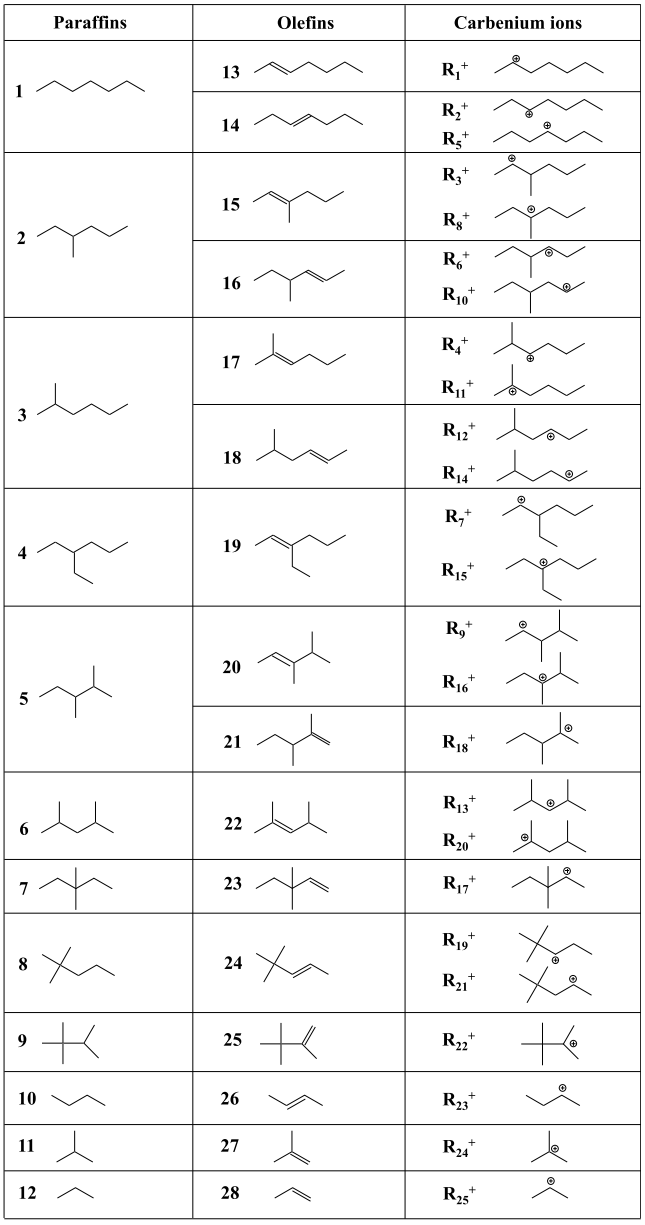

Figure 11. Chemical species selected for the reduced reaction scheme, showing the correspondence between paraffins, olefins, and related carbenium ions.

of the B_2 cracking as the reactant (secondary carbenium ion) is less stable in the former case than in the latter one (tertiary cation). With the barrier for B_2 being as high as 84 kJ·mol^{-1} and the free energy difference between a secondary versus tertiary cation being about 60 kJ·mol^{-1} (from the protonation energy difference, Table S2, assuming similar free energy for all adsorbed olefins), an estimate of the type C cracking free energy barrier is 24 kJ·mol^{-1}. Moreover, whereas we can propose values for the activation Gibbs free energy for cracking reactions from first-principles calculations, we do not have their enthalpy versus entropy partitioning. So far, we have assumed an activation entropy of zero. Table 1 gives the whole set of kinetic constants used for the 45 reactions.

3.3.2. Comparison with Experimental Results. Comparisons with experiments were made on the conversion of *n*-heptane, the isomerization and cracking yields, and the composition of the different groups of isomers (mono-, di-,

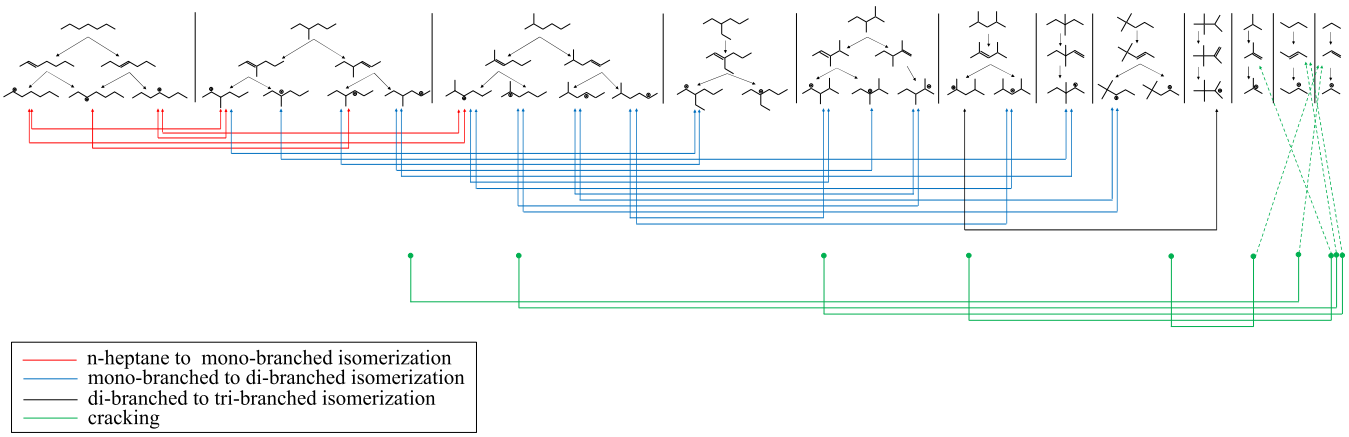

Figure 12. Hydrocracking of *n*-heptane: reduced reaction network considered for the kinetic modeling (chemical species are the same as those depicted in Figure 11).

Table 1. Kinetic Parameters Assigned to the Different Reactions[a]

reaction number	reaction type	number of branches	$\Delta_r H^{\ddagger}$ (kJ/mol)	$\Delta_r S^{\ddagger}$ (J/mol/K)
1/2/3	s−s type B isom.	linear → monobranched	24.3	−21.9
4/5/6	s−s type B isom.	monobranched → dibranched	25.2	−17.6
7/8	s−s type B isom.	linear → monobranched	24.3	−21.9
9	s−s type B isom.	monobranched → dibranched	25.2	−17.6
10	t−t type B isom.	monobranched → dibranched	69	−38.3
11	t−s type B isom.	monobranched → dibranched	$k = 0\ s^{-1}$	
12	s−s type B isom.	monobranched → dibranched	25.2	−17.6
13	s−t type B isom.	monobranched → dibranched	13.4	−32.6
14	t−t type B isom.	monobranched → dibranched	69	−38.3
15	t−s type B isom.	monobranched → dibranched	$k = 0\ s^{-1}$	
16	s−s type B isom.	monobranched → dibranched	25.2	−17.6
17	s−t type B isom.	monobranched → dibranched	13.4	−32.6
18/19	s−s type B isom.	monobranched → dibranched	25.2	−17.6
20	t−t type B isom.	dibranched → tribranched	67	−31
21/22/23	s−s type B isom.	monobranched → linear	32.6	−23.1
24/25/26	s−s type B isom.	dibranched → monobranched	31.1	−21.8
27/28	s−s type B isom.	monobranched → linear	32.6	−23.1
29	s−s type B isom.	dibranched → monobranched	31	−21.8
30	t−t type B isom.	dibranched → monobranched	71.8	−28.6
31	s−t type B isom.	dibranched → monobranched	$k = 0\ s^{-1}$	
32	s−s type B isom.	dibranched → monobranched	31	−21.8
33	t−s type B isom.	dibranched → monobranched	75.4	−28.1
34	t−t type B isom.	dibranched → monobranched	71.8	−28.6
35	s−t type B isom.	dibranched → monobranched	$k = 0\ s^{-1}$	
36	s−s type B isom.	dibranched → monobranched	31	−21.8
37	t−s type B isom.	dibranched → monobranched	75.4	−28.1
38/39	s−s type B isom.	dibranched → monobranched	31	−21.8
40	t−t type B isom.	tribranched → dibranched	71.3	−32.6
41*/42*/43*	s−s cracking		40	0
44*	t−s cracking		93	0
45*	s−t cracking		40	0

[a]The numbering of the reactions is given in Figure S7. Secondary and tertiary cations are denoted as s and t, respectively. Reactions denoted with an asterisk have been adjusted with respect to the DFT data (see Table 2).

and tribranched paraffins). Figure 13 shows the evolution of the simulated and experimental conversion of *n*-heptane as a function of space time for three temperatures (220, 230, and 240 °C). Few inaccurate parameters have been modified manually to obtain a better fit between the model and experiments (Table 2). In particular, the adsorption free energy of the olefins seems to be underestimated by the DFT calculation (−28 instead of 0 kJ·mol^{-1} for all temperatures). This parameter was adjusted to render the evolution of the activity with respect to the temperature. The first-principles evaluation was done based on a static PBE + D2 calculation. Our modification of the adsorption free energy is thus compatible with recent findings according to which PBE + D2 underestimates the adsorption energy of hydrocarbons (too negative values are computed) compared to higher levels of theory [such as MP2/CCSD(T)].[63] We note that although

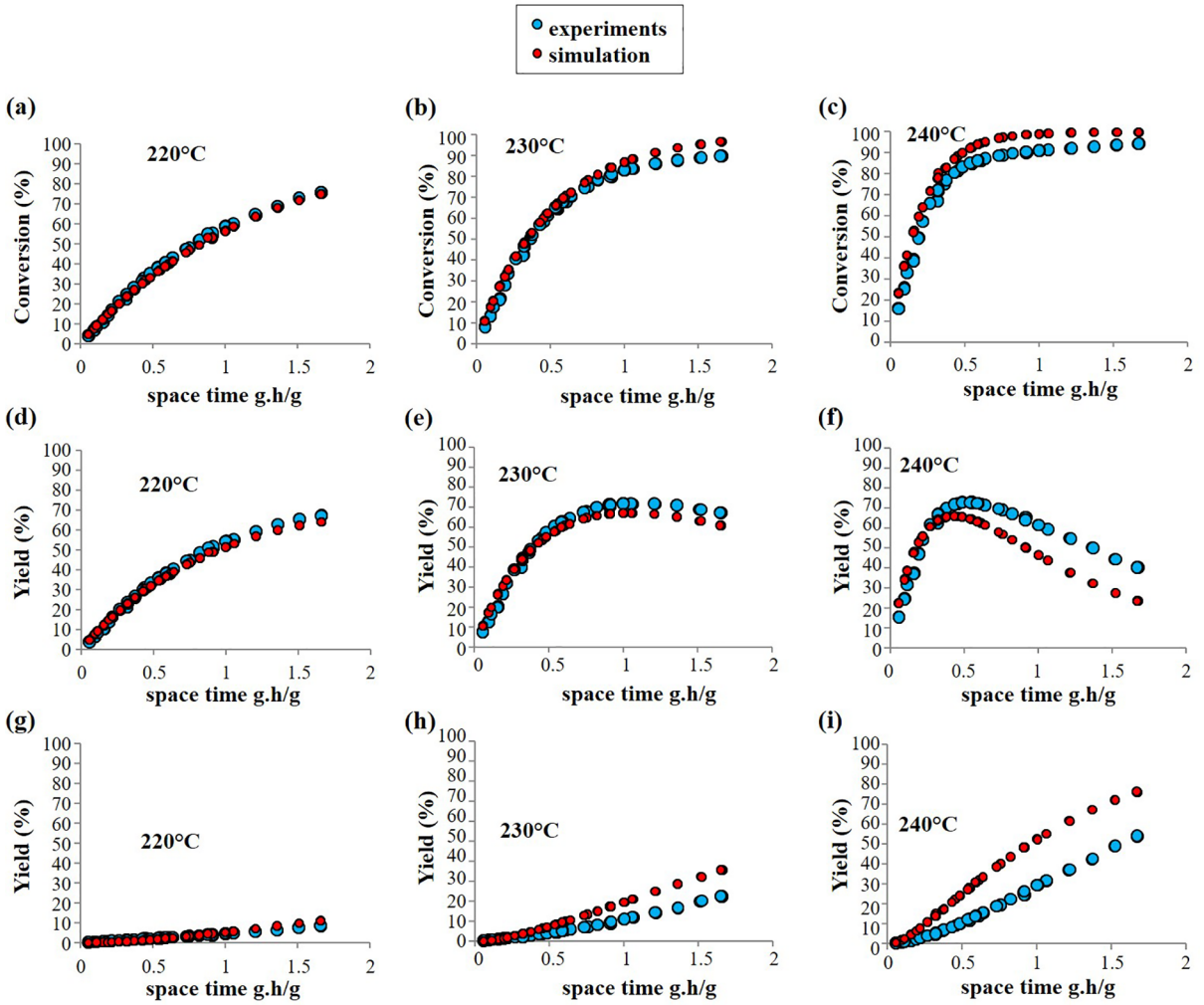

Figure 13. Comparison of the modeled and experimental conversion (a–c), isomerization (d–f), and cracking (g–i) yields at 220 °C (a,d,g), 230 °C (b,e,h), and 240 °C (c,f,i).

Table 2. Parameters Adjusted during Kinetic Modeling Using Data Measured at 220 °C as the Reference

data	original value	adjusted value
C^{A}_{site} (acid-site concentration) (μmol g^{-1})	116	35
$\Delta_t G_{ads}$(olefins) (kJ·mol^{-1})	−28	0
$\Delta G_{+}^{\ddagger}$ (type C cracking) (kJ·mol^{-1})	24	40
$\Delta G_{+}^{\ddagger}$ (type B1 cracking) (kJ·mol^{-1})	15	30
$\Delta G_{+}^{\ddagger}$ (type B2 cracking) (kJ·mol^{-1})	84	93

the shorter products are likely to have different adsorption energies than the longer ones, any modification of the values for the C3 and C4 compounds cannot have any impact on the predicted activity and selectivity because the cracking reactions were considered as irreversible in our kinetic model.

In addition, the concentration of accessible acid sites (C^{A}_{site} in eq 3) is also highly uncertain, as discussed in Section 2.1.1. The total acid site concentration was set to 35 μmol g^{-1} to be in the order of magnitude of the observed experimental activity. This is much lower than the amounts deduced from the combination of XRF and NMR (810 μmol g^{-1}, by a factor of 23) or pyridine adsorption monitored by FTIR spectroscopy (116 μmol g^{-1}, by a factor of 3). This means that not all sites are able to protonate pyridine, after thermodesorption of the latter at 150 °C, and that not all the sites able to protonate pyridine in these conditions are able to convert C7 alkenes in the 220–240 °C temperature range. Notably, as the change made on the adsorption free energy is not temperature-dependent, its effects are effectively equivalent to a decrease in the number of active sites. Thus, it is currently not possible to deconvolute these two effects.

Moreover, a modification of the Gibbs free energy of activation of type C, B_1, and B_2 cracking steps was performed to recover the cracking product selectivity. Those modifications (at most 15 kJ·mol^{-1}) remain within the uncertainty of the ab initio calculations. It is interesting to note that the deviation between the GGA + D2 estimation (from AIMD) is systematic: the first-principles evaluation is always slightly too low. This may be linked to some previous observations indicating that GGA underestimates barriers for several kinds of hydrocarbon transformations, more or less severely depending on the reaction.[63,64] To the best of our knowledge, alkene cracking reactions are not as well benchmarked with respect to the level of theory upon comparing to alkane cracking, for example.[63] Regarding the cracking yields, the agreement is satisfactory for 220 °C, while small deviations are observed at high temperature. This is likely linked to the absence of knowledge on the enthalpy versus entropy partitioning in the free-energy barrier that could be better described in the future. Whereas the deviation of intrinsic

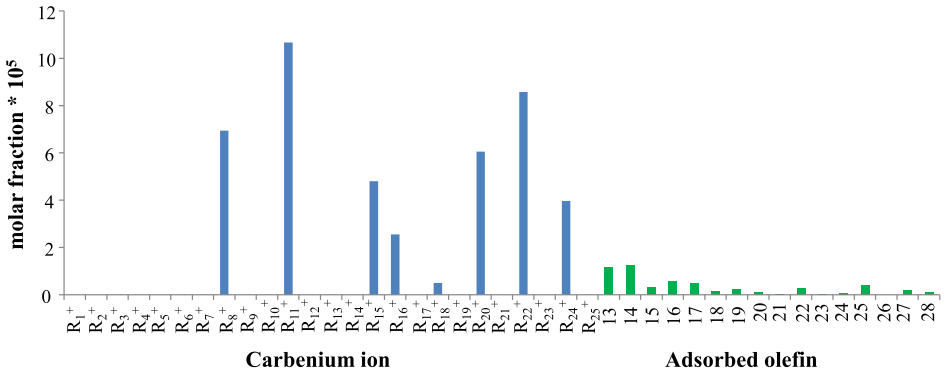

Figure 14. Simulated coverage molar ratio of carbenium ions and adsorbed olefins for a space time of 1.66 g·h/g at 220 °C. The labeling of the species refers to Figure 11.

cracking barriers remains moderate, the effects on the apparent barriers are, due to the cumulation of systematic errors in the prediction of adsorption energies and intrinsic barriers, likely to be larger than 40 kJ·mol^{-1}. We remark, however, that a caution has to be taken when evaluating the adsorption free energy change with respect to the change in the number of acid sites (see above).

In the end, good agreement between the modeled and experimental results can be seen in Figure 13. Figures 7 and 8 show the relative molar compositions at 220 °C of the monobranched and dibranched paraffin families, respectively. It can be noticed that monobranched paraffins are in thermodynamic equilibrium regardless of the residence time. On the other hand, for dibranched paraffins, it is necessary to have a long residence time to reach the thermodynamic equilibrium (space time > 0.6 g·h/g). The equilibrium determined by tabulation and the one obtained experimentally are different. This is probably due to the uncertainty of the thermodynamic table used.[65] For low residence time, dibranched isomers do not have enough time to be equilibrated. However, due to the equilibrium assumptions explicitly built in the model for paraffins with the same number of branches, the equilibration violation cannot be predicted by the model.

3.3.3. Coverage of Reaction Intermediates. The simulated coverage of carbenium ions and adsorbed olefins was computed (Figure 14). The coverage of free sites (higher than 0.99997, whatever the space time) is high, meaning that only a very small fraction of the acid sites (C^A_{site}) is bound to carbenium or olefins, in agreement with previous findings from traditional single-event modeling[2,3] and first-principles kinetic modeling for cycloalkane hydroisomerization.[16] Regarding the adsorbed species, only tertiary ions appear in significant concentrations. This result agrees with the greater stability of these ions with respect to secondary carbenium ions.

Another interesting remark can be made concerning the high coverage ratio of olefin 2-heptene compared to the olefin coverage ratio and the low coverage ratio of the corresponding ion (R_1^+, terminology in Figure 11) compared to the others. This shows clearly that the corresponding secondary carbenium ions are, due to their low stability, formed at trace amounts even if the abundance of the olefin is high. This is a consequence of the relative free energies of secondary cations with respect to their corresponding π-complexes, showing that relevant intermediates are olefins instead of secondary cations as found also for cycloalkenes.[16] Notably, the R_{19}^+ and R_{17}^+ cations, the formation of which was not found to be possible by DFT calculations, are formed at extremely low amounts, as well as the corresponding π-complexes, whereas R_{16}^+ (expected to be formed instead of R_{17}^+) and R_{18}^+ (expected to be formed instead of R_{19}^+) are much more abundant. Within cracked products, adsorbed isobutenium R_{24}^+ dominates over linear butenium (R_{23}^+) and propenium (R_{25}^+). This is in line with the lower type B_1 barrier that produces it, as compared to B_2 and C cracking types. This is also fully in line with C_4 product yields, with isobutane being dominant over *n*-butane, as illustrated in Figure S6.

4. CONCLUSIONS

The optimization of predictive kinetic models for catalytic processes is a complex task, in particular for the hydroconversion of alkanes on acid-limited bifunctional catalysts, owing to the size of the reaction network and because of the difficulty in obtaining independent data such as the rate and equilibrium constants for the various kinds of reactions involved in the zeolite catalyst (alkene adsorption, protonation, isomerization, and cracking). Thanks to a combination of DFT calculations and multiscale single-event microkinetic modeling based on the data obtained by DFT (both obtained by static methods and AIMD), a predictive model for *n*-heptane hydroconversion in large-pore zeolites has been obtained. It was validated by kinetic HTE performed with a well-balanced Pt/Beta catalyst.

HTE experiments allow the acquisition of a large set of kinetic data that substantiate an apparent mechanism linking linear, monobranched, dibranched, and tribranched heptenes, followed by the cracking of mono- and dibranched isomers. DFT calculations show that secondary cations are much less stable than tertiary ones and adsorbed alkenes. This is of prime importance in the quantification of type B isomerization reaction barriers, depending on the type of the carbenium ion. Cracking reaction barriers are also strongly affected by the nature of the cation that cracks and that of the cracking products.

The agreement between the simulated and experimental kinetic data is good, showing the reliability of the multiscale kinetic approach, avoiding the simultaneous fit of dozens of thermokinetic parameters. The hypothesis of equilibrium within the monobranched family, used in the kinetic model, is proven to be reasonable in most cases, with exception of dibranched species, where this hypothesis is debatable. Only a few parameters were adjusted to improve the correspondence with the experiments. The number of active acid sites had to be strongly decreased by a factor of more than 3 to reproduce

conversion levels, showing that only a fraction of acid sites measured by XRF/NMR or probed by pyridine catalyzes the reaction at temperature higher than 220 °C. Cracking barriers were increased by about 15 kJ·mol^{-1}, suggesting a possible effect of the level of theory employed for the prediction of the corresponding rate constants. The free energy of the adsorption of olefins could also be refined in the future, ideally with the aid of AIMD. Isomerization barriers evaluated by DFT calculations were kept unaltered. The analysis of the simulated coverage demonstrated that a very small proportion of acid sites is involved in the alkene adsorption and further reactions in the relevant experimental conditions. When these reactions occur, tertiary carbenium ion intermediates appear at significantly higher concentration than the other species.

Overall, the approach developed in the present work is highly promising for the prediction of catalytic performance, giving a molecular basis to assumptions made in kinetic modeling and removing the biggest part of the usual fitting approach. The model obtained in the present work is likely transposable to most of the large-pore zeolites in the bifunctional hydroisomerization of *n*-heptane and may serve as a basis for the prediction of the behavior of longer-chain alkanes of relevance for the catalytic transformation of conventional hydrocarbon sources and of renewables. The model can still be improved in the future. For instance, the cracking reactions starting from tertiary carbenium ions and producing other tertiary cations have not been considered in the present study, although they come into play for longer chains. To the best of our knowledge, our work represents the first report on such a multiscale approach for this complex reaction network. We show that combining these techniques leads to a successful description that is promising for the extension of the method to other catalytic systems.

Limitation of the reaction kinetics by the acidic phase, validation of HTE kinetic experiments, complete reaction network for *n*-heptane hydrocracking, complementary experimental catalytic features, kinetic data obtained from DFT calculations, and details for the kinetic modeling approach (PDF)

AUTHOR INFORMATION

Corresponding Authors

Jean-Marc Schweitzer − *IFP Energies nouvelles—Rond-Point de l'Echangeur de Solaize—BP 3, 69360 Solaize, France*; Email: jean-marc.schweitzer@ifpen.fr

Céline Chizallet − *IFP Energies nouvelles—Rond-Point de l'Echangeur de Solaize—BP 3, 69360 Solaize, France*; orcid.org/0000-0001-5140-8397; Email: celine.chizallet@ifpen.fr

Authors

Jérôme Rey − *IFP Energies nouvelles—Rond-Point de l'Echangeur de Solaize—BP 3, 69360 Solaize, France*

Charles Bignaud − *IFP Energies nouvelles—Rond-Point de l'Echangeur de Solaize—BP 3, 69360 Solaize, France; Département de Chimie, PSL University, 75005 Paris, France*

Tomáš Bučko − *Department of Physical and Theoretical Chemistry, Faculty of Natural Sciences, Comenius University in Bratislava, SK- 84215 Bratislava, Slovakia; Institute of Inorganic Chemistry, Slovak Academy of Sciences, SK-84236 Bratislava, Slovakia;* orcid.org/0000-0002-5847-9478

Pascal Raybaud − *IFP Energies nouvelles—Rond-Point de l'Echangeur de Solaize—BP 3, 69360 Solaize, France;* orcid.org/0000-0003-4506-5062

Maïlys Moscovici-Mirande − *IFP Energies nouvelles—Rond-Point de l'Echangeur de Solaize—BP 3, 69360 Solaize, France*

Frédéric Portejoie − *IFP Energies nouvelles—Rond-Point de l'Echangeur de Solaize—BP 3, 69360 Solaize, France*

Christophe James − *IFP Energies nouvelles—Rond-Point de l'Echangeur de Solaize—BP 3, 69360 Solaize, France*

Christophe Bouchy − *IFP Energies nouvelles—Rond-Point de l'Echangeur de Solaize—BP 3, 69360 Solaize, France*

Notes

The authors declare no competing financial interest.

ACKNOWLEDGMENTS

HPC resources were used from GENCI-IDRIS (grant A0060806134) and IFPEN (ENER440). T.B. acknowledges support from the Slovak Research and Development Agency (contracts no. APVV−20−0127 and no. VEGA-1/0777/19).

NOMENCLATURE

F_i^g molar flow rate of compound i in the gas phase [mol/m^3]
C_{site}^A total concentration of the acidic sites in the zeolite [mol/kg]
r_j reaction rate of reaction j [s^{-1}]
S_r reactor section [m^2]
z axial position in the reactor [m]
$K_{ads}^{O_i}$ adsorption equilibrium constant for olefin O_i [-]

GREEK SYMBOLS

ε_s solid holdup [-]
ρ_s solid grain density [kg/m^3]
μ_{ij} stoichiometric coefficients of compound i in reaction j [-]

REFERENCES

(1) de Oliveira, L. P.; Hudebine, D.; Guillaume, D.; Verstraete, J. J. A Review of Kinetic Modeling Methodologies for Complex Processes. *Oil Gas Sci. Technol* **2016**, *71*, 45.

(2) Martens, G. G.; Marin, G. B.; Martens, J. A.; Jacobs, P. A.; Baron, G. V. A Fundamental Kinetic Model for Hydrocracking of C8 to C12 Alkanes on Pt/US-Y Zeolites. *J. Catal.* **2000**, *195*, 253−267.

(3) Thybaut, J. W.; Marin, G. B.; Baron, G. V.; Jacobs, P. A.; Martens, J. A. Alkene Protonation Enthalpy Determination from Fundamental Kinetic Modeling of Alkane Hydroconversion on Pt/H-(US)Y-Zeolite. *J. Catal.* **2001**, *202*, 324−339.

(4) Thybaut, J. W.; Narasimhan, C. S. L.; Marin, G. B.; Denayer, J. F. M.; Baron, G. V.; Jacobs, P. A.; Martens, J. A. Alkylcarbenium Ion Concentrations in Zeolite Pores During Octane Hydrocracking on Pt/H-USY Zeolite. *Catal. Lett.* **2004**, *94*, 81−88.

(5) Surla, K.; Guillaume, D.; Verstraete, J. J.; Galtier, P. Kinetic Modeling using the Single-Event Methodology: Application to the Isomerization of Light Paraffins. *Oil Gas Sci. Technol* **2011**, *66*, 343−365.
(6) van Santen, R. A.; Sautet, P. *Computational Methods in Catalysis and Materials Science*; Wiley-VCH: Weinheim, 2009.
(7) Salciccioli, M.; Stamatakis, M.; Caratzoulas, S.; Vlachos, D. G. A Review of Multiscale Modeling of Metal-Catalyzed Reactions: Mechanism Development for Complexity and Emergent Behavior. *Chem. Eng. Sci.* **2011**, *66*, 4319−4355.
(8) Larmier, K.; Nicolle, A.; Chizallet, C.; Cadran, N.; Maury, S.; Lamic-Humblot, A.-F.; Marceau, E.; Lauron-Pernot, H. Influence of Coadsorbed Water and Alcohol Molecules on Isopropyl Alcohol Dehydration on γ-Alumina: Multiscale Modeling of Experimental Kinetic Profiles. *ACS Catal.* **2016**, *6*, 1905−1920.
(9) Sabbe, M. K.; Canduela-Rodriguez, G.; Joly, J.-F.; Reyniers, M.-F.; Marin, G. B. Ab Initio Coverage-Dependent Microkinetic Modeling of Benzene Hydrogenation on Pd(111). *Catal. Sci. Technol.* **2017**, *7*, 5267−5283.
(10) Bruix, A.; Margraf, J. T.; Andersen, M.; Reuter, K. First-Principles-Based Multiscale Modelling of Heterogeneous Catalysis. *Nat. Catal.* **2019**, *2*, 659−670.
(11) John, M.; Alexopoulos, K.; Reyniers, M.-F.; Marin, G. B. Reaction Path Analysis for 1-Butanol Dehydration in H-ZSM-5 Zeolite: Ab Initio and Microkinetic Modeling. *J. Catal.* **2015**, *330*, 28−45.
(12) John, M.; Alexopoulos, K.; Reyniers, M.-F.; Marin, G. B. Effect of Zeolite Confinement on the Conversion of 1-Butanol to Butene Isomers: Mechanistic Insights from DFT Based Microkinetic Modelling. *Catal. Sci. Technol.* **2017**, *7*, 2978−2997.
(13) John, M.; Alexopoulos, K.; Reyniers, M.-F.; Marin, G. B. Mechanistic Insights into the Formation of Butene Isomers from 1-Butanol in H-ZSM-5: DFT based Microkinetic Modelling. *Catal. Sci. Technol.* **2017**, *7*, 1055−1072.
(14) Liu, C.; van Santen, R. A.; Poursaeidesfahani, A.; Vlugt, T. J. H.; Pidko, E. A.; Hensen, E. J. M. Hydride Transfer versus Deprotonation Kinetics in the Isobutane-Propene Alkylation Reaction: A Computational Study. *ACS Catal.* **2017**, *7*, 8613−8627.
(15) Plessow, P. N.; Smith, A.; Tischer, S.; Studt, F. Identification of the Reaction Sequence of the MTO Initiation Mechanism Using Ab Initio-Based Kinetics. *J. Am. Chem. Soc.* **2019**, *141*, 5908−5915.
(16) Gutierrez-Acebo, E.; Rey, J.; Bouchy, C.; Schuurman, Y.; Chizallet, C. Ab initio-based Kinetic Modelling of Ethylcyclohexane Hydroisomerization Sheds New Light on the Relevant Reaction Intermediates. *ChemCatChem* **2021**, *13*, 3434−3442.
(17) Marcilly, C. *Acido-Basic Catalysis*; Technip: Paris, 2005.
(18) Bertoncini, F.; Bonduelle-Skrzypcak, A.; Francis, J.; Guillon, E. Hydrocracking. In *Catalysis by transition metal sulphides: from molecular theory to industrial applications*; Toulhoat, H., Raybaud, P., Eds.; Editions Technip, 2013, pp 609−677.
(19) Bouchy, C.; Hastoy, G.; Guillon, E.; Martens, J. A. Fischer-Tropsch Waxes UpgradingviaHydrocracking and Selective Hydroisomerization. *Oil Gas Sci. Technol* **2009**, *64*, 91−112.
(20) Martens, J. A.; Verboekend, D.; Thomas, K.; Vanbutsele, G.; Gilson, J.-P.; Pérez-Ramírez, J. Hydroisomerization of Emerging Renewable Hydrocarbons using Hierarchical Pt/H-ZSM-22 Catalyst. *ChemSusChem* **2013**, *6*, 421−425.
(21) Martens, J. A.; Tielen, M.; Jacobs, P. A.; Weitkamp, J. Estimation of the Void Structure and Pore Dimensions of Molecular Sieve Zeolites using the Hydroconversion of n-Decane. *Zeolites* **1984**, *4*, 98−107.
(22) Weitkamp, J. Catalytic Hydrocracking-Mechanisms and Versatility of the Process. *ChemCatChem* **2012**, *4*, 292−306.
(23) Patrigeon, A.; Benazzi, E.; Travers, C.; Bernhard, J. Y. Influence of the Zeolite Structure and Acidity on the Hydroisomerization of n-Heptane. *Catal. Today* **2001**, *65*, 149−155.
(24) Oenema, J.; Harmel, J.; Vélez, R. P.; Meijerink, M. J.; Eijsvogel, W.; Poursaeidesfahani, A.; Vlugt, T. J. H.; Zečević, J.; de Jong, K. P. Influence of Nanoscale Intimacy and Zeolite Micropore Size on the Performance of Bifunctional Catalysts for n-Heptane Hydroisomerization. *ACS Catal.* **2020**, *10*, 14245−14257.
(25) Poursaeidesfahani, A.; de Lange, M. F.; Khodadadian, F.; Dubbeldam, D.; Rigutto, M.; Nair, N.; Vlugt, T. J. H. Product Shape Selectivity of MFI-Type, MEL-Type, and BEA-Type Zeolites in the Catalytic Hydroconversion of Heptane. *J. Catal.* **2017**, *353*, 54−62.
(26) Samad, J. E.; Blanchard, J.; Sayag, C.; Louis, C.; Regalbuto, J. R. The Controlled Synthesis of Metal-Acid Bifunctional Catalysts: The Effect of Metal:Acid Ratio and Metal-Acid Proximity in Pt Silica-Alumina Catalysts for n-Heptane Isomerization. *J. Catal.* **2016**, *342*, 203−212.
(27) Zecevic, J.; Vanbutsele, G.; de Jong, K. P.; Martens, J. A. Nanoscale Intimacy in Bifunctional Catalysts for Selective Conversion of Hydrocarbons. *Nature* **2015**, *528*, 245−248.
(28) Rigby, A. M.; Kramer, G. J.; van Santen, R. A. Mechanisms of Hydrocarbon Conversion in Zeolites: A Quantum Mechanical Study. *J. Catal.* **1997**, *170*, 1−10.
(29) Boronat, M.; Viruela, P. M.; Corma, A. Reaction Intermediates in Acid Catalysis by Zeolites: Prediction of the Relative Tendency To Form Alkoxides or Carbocations as a Function of Hydrocarbon Nature and Active Site Structure. *J. Am. Chem. Soc.* **2004**, *126*, 3300−3309.
(30) Viruela-Martin, P.; Zicovich-Wilson, C. M.; Corma, A. Ab initio molecular orbital calculations of the protonation of propylene and isobutene by acidic hydroxyl groups of isomorphously substituted zeolites. *J. Phys. Chem.* **1993**, *97*, 13713−13719.
(31) Ren, Q.; Rybicki, M.; Sauer, J. Interaction of C3-C5 Alkenes with Zeolitic Brønsted Sites: π-Complexes, Alkoxides, and Carbenium Ions in H-FER. *J. Phys. Chem. C* **2020**, *124*, 10067−10078.
(32) Leydier, F.; Chizallet, C.; Costa, D.; Raybaud, P. Revisiting Carbenium Chemistry on Amorphous Silica-Alumina: Unraveling their Milder Acidity as Compared to Zeolites. *J. Catal.* **2015**, *325*, 35−47.
(33) Cnudde, P.; De Wispelaere, K.; Vanduyfhuys, L.; Demuynck, R.; Van der Mynsbrugge, J.; Waroquier, M.; Van Speybroeck, V. How Chain Length and Branching Influence the Alkene Cracking Reactivity on H-ZSM-5. *ACS Catal.* **2018**, *8*, 9579−9595.
(34) Cnudde, P.; De Wispelaere, K.; Van der Mynsbrugge, J.; Waroquier, M.; Van Speybroeck, V. Effect of Temperature and Branching on the Nature and Stability of Alkene Cracking Intermediates in H-ZSM-5. *J. Catal.* **2017**, *345*, 53−69.
(35) Rey, J.; Bignaud, C.; Raybaud, P.; Bučko, T.; Chizallet, C. Dynamic Features of Transition States for β-Scission Reactions of Alkenes over Acid Zeolites Revealed by AIMD Simulations. *Angew. Chem., Int. Ed.* **2020**, *59*, 18938−18942.
(36) Tuma, C.; Kerber, T.; Sauer, J. The tert-Butyl Cation in H-Zeolites: Deprotonation to Isobutene and Conversion into Surface Alkoxides. *Angew. Chem., Int. Ed.* **2010**, *49*, 4678−4680.
(37) Tuma, C.; Sauer, J. Protonated Isobutene in Zeolites:tert-Butyl Cation or Alkoxide? *Angew. Chem., Int. Ed.* **2005**, *44*, 4769−4771.
(38) Brouwer, D. M.; Hogeveen, H. Electrophilic Substitutions at Alkanes and in Alkylcarbonium Ions. *Prog. Phys. Org. Chem.* **1972**, *9*, 179−240.
(39) Rey, J.; Raybaud, P.; Chizallet, C.; Bučko, T. Competition of Secondary versus Tertiary Carbenium Routes for the Type B Isomerization of Alkenes over Acid Zeolites Quantified by Ab Initio Molecular Dynamics Simulations. *ACS Catal.* **2019**, *9*, 9813−9828.
(40) Rey, J.; Gomez, A.; Raybaud, P.; Chizallet, C.; Bučko, T. On the Origin of the Difference between Type A and Type B Skeletal Isomerization of Alkenes Catalyzed by Zeolites: The Crucial Input of Ab Initio Molecular Dynamics. *J. Catal.* **2019**, *373*, 361−373.
(41) Weitkamp, J.; Jacobs, P. A.; Martens, J. A. Isomerization and Hydrocracking of C9 through C16 n-Alkanes on Pt/HZSM-5 Zeolite. *Appl. Catal.* **1983**, *8*, 123−141.
(42) Raybaud, P.; Patrigeon, A.; Toulhoat, H. The Origin of the C7-Hydroconversion Selectivities on Y, β, ZSM-22, ZSM-23, and EU-1 Zeolites. *J. Catal.* **2001**, *197*, 98−112.
(43) Gutierrez-Acebo, E.; Leroux, C.; Chizallet, C.; Schuurman, Y.; Bouchy, C. Metal/Acid Bifunctional Catalysis and Intimacy Criterion

for Ethylcyclohexane Hydroconversion: When Proximity Does Not Matter. *ACS Catal.* **2018**, *8*, 6035−6046.
(44) Emeis, C. A. Determination of Integrated Molar Extinction Coefficients for Infrared Absorption Bands of Pyridine Adsorbed on Solid Acid Catalysts. *J. Catal.* **1993**, *141*, 347−354.
(45) Perdew, J. P.; Burke, K.; Ernzerhof, M. Generalized Gradient Approximation Made Simple. *Phys. Rev. Lett.* **1996**, *77*, 3865−3868.
(46) Kresse, G.; Hafner, J. Ab initiomolecular-dynamics simulation of the liquid-metal-amorphous-semiconductor transition in germanium. *Phys. Rev. B* **1994**, *49*, 14251−14269.
(47) Kresse, G.; Furthmüller, J. Efficiency of Ab-Initio Total Energy Calculations for Metals and Semiconductors using a Plane-Wave Basis Set. *Comput. Mater. Sci.* **1996**, *6*, 15−50.
(48) Kresse, G.; Joubert, D. From Ultrasoft Pseudopotentials to the Projector Augmented-Wave Method. *Phys. Rev. B* **1999**, *59*, 1758−1775.
(49) Grimme, S. Semiempirical GGA-Type Density Functional Constructed with a Long-Range Dispersion Correction. *J. Comput. Chem.* **2006**, *27*, 1787−1799.
(50) Henkelman, G.; Jónsson, H. A Dimer Method for Finding Saddle Points on High Dimensional Potential Surfaces using only First Derivatives. *J. Chem. Phys.* **1999**, *111*, 7010−7022.
(51) Heyden, A.; Bell, A. T.; Keil, F. J. Efficient Methods for Finding Transition States in Chemical Reactions: Comparison of Improved Dimer Method and Partitioned Rational Function Optimization Method. *J. Chem. Phys.* **2005**, *123*, 224101.
(52) Fukui, K. The Path of Chemical Reactions - the IRC Approach. *Acc. Chem. Res.* **1981**, *14*, 363−368.
(53) Fukui, K. Formulation of the Reaction Coordinate. *J. Phys. Chem.* **1970**, *74*, 4161−4163.
(54) Hratchian, H. P.; Schlegel, H. B. Following Reaction Pathways Using a Damped Classical Trajectory Algorithm. *J. Phys. Chem. A* **2002**, *106*, 165−169.
(55) Jensen, F. *Introduction to Computational Chemistry*; 2nd ed. ed.; John Wiley & Sons: Chichester England; Hoboken NJ, 2007.
(56) Eyring, H. The Activated Complex in Chemical Reactions. *J. Chem. Phys.* **1935**, *3*, 107−115.
(57) Feng, W.; Vynckier, E.; Froment, G. F. Single Event Kinetics of Catalytic Cracking. *Ind. Eng. Chem. Res.* **1993**, *32*, 2997−3005.
(58) Schweitzer, J.-M.; Galtier, P.; Schweich, D. A Single Events Kinetic Model for the Hydrocracking of Paraffins in a Three-Phase Reactor. *Chem. Eng. Sci.* **1999**, *54*, 2441−2452.
(59) Froment, G. F. Single Event Kinetic Modeling of Complex Catalytic Processes. *Catal. Rev.* **2005**, *47*, 83−124.
(60) Trambouze, P.; Euzen, J. P. *Les réacteurs chimiques. De la conception à la mise en oeuvre*; Technip: Paris, 2002.
(61) Froment, G. F.; Bischoff, F. *Chemical Reactor Analysis and Design*, 2nd ed.; John Wiley & Sons: New York, Chichester, Brisbane, 1990.
(62) Patrigeon, A. *PhD Thesis*; Montpellier II - IFP, 2000.
(63) Berger, F.; Rybicki, M.; Sauer, J. Adsorption and Cracking of Propane by Zeolites of Different Pore Size. *J. Catal.* **2021**, *395*, 117−128.
(64) Goncalves, T. J.; Plessow, P. N.; Studt, F. On the Accuracy of Density Functional Theory in Zeolite Catalysis. *ChemCatChem* **2019**, *11*, 4368−4376.
(65) Benson, S. W.; Buss, J. H. Additivity Rules for the Estimation of Molecular Properties. Thermodynamic Properties. *J. Chem. Phys.* **1958**, *29*, 546−572.